Synergistically catalytic enhanced of Zn–N/Co–N dual active sites as highly efficient and durable bifunctional electrocatalyst for rechargeable zinc-air battery

Mancai Qian [a,1], Meijiao Xu [a,1], Man Guo [a], Tayirjan Taylor Isimjan [c,**], Elvis Shoko [d], Zhongfeng Shi [b,***], Xiulin Yang [a,*]

[a] Guangxi Key Laboratory of Low Carbon Energy Materials, School of Chemistry and Pharmaceutical Sciences, Guangxi Normal University, Guilin, 541004, China
[b] College of Chemistry and Chemical Engineering, Beibu Gulf University, Qinzhou, 535000, China
[c] Saudi Arabia Basic Industries Corporation (SABIC) at King Abdullah University of Science and Technology (KAUST), Thuwal, 23955-6900, Saudi Arabia
[d] Department of Chemistry, University of Liverpool, Liverpool, L69 3BX, United Kingdom

HIGHLIGHTS

- Quaternary Zn–Co–N–S co-doped tubular carbon is fabricated by a controllable strategy.
- The high porosity of the catalyst provides fast mass transfer and more active sites.
- The catalyst exhibits long-term stability for rechargeable zinc-air batteries.
- The synergy between different components dominates the outstanding performance.

GRAPHICAL ABSTRACT
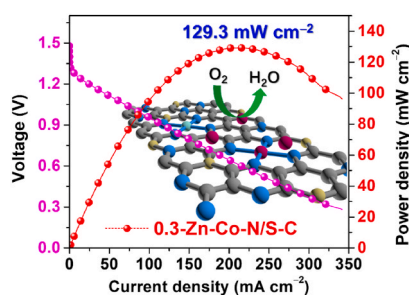
ARTICLE INFO

ABSTRACT

The theoretical energy density, stability and cost of Zn-air batteries (ZAB) are far inferior to the most advanced lithium-ion batteries due to the irreversibility of zinc electrodes and sluggish electrocatalytic performance of oxygen reduction (ORR) and oxygen evolution (OER) processes. Herein, we designed a simple strategy to fabricate a quaternary Zn–Co–N–S co-doped tubular carbon (0.3-Zn-Co-N/S–C) via direct pyrolysis of various mixtures of precursors. The high porosity of 3D nanostructure not only provides better mass transfer but also offers a large number of active sites thereof superior ORR and OER performances. As a result, the rechargeable ZAB fabricated using optimized 0.3-Zn-Co-N/S–C as cathode exhibited a higher open-circuit voltage, stable discharge rate, and better reversibility, even exceeding the state-of-the-art Pt/C catalyst in alkaline solution. The catalytic mechanism indicates that the synergistic effect of Co metal nanoparticles, Co–N/Zn–N active sites, and the high-yield of N/S-doped tubular carbon dominate the outstanding catalytic performance.

1. Introduction

Developing high-performance bifunctional electrocatalysts as an anode is the key to achieving an efficient rechargeable Zn-air battery (ZAB). The goal of developing a bifunctional cathode is to overcome the decay/failure in an alkaline condition resulted from dendrite formation, undesired relocation, and zinc oxide passivation. In general, these problems are likely to be tackled through improving porosity and conductivity by adding heavy metals, carbon, and a surfactant or surface modification and morphology optimization. The strategies include direct inhibition/suppression, designing 3D conductive host, and constructing high-surface-area porous structures [1].

Electrochemical oxygen reduction reaction (ORR) and oxygen evaluation reaction (OER) are two basic reactions for rechargeable ZAB where the ORR happens during the charge release and OER occurs during the charging. Both ORR and OER are the reactions in electrochemical energy storage and energy conversion process, such as fuel cells and metal-air batteries [2,3]. However, the intrinsically slow kinetics with multi-electron and multi-proton transfer requires efficient electrocatalysts to reduce reaction overpotential and accelerate reaction [4]. To date, although the platinum group metal-based electrocatalysts show high catalytic activity of ORR/OER and have been used in commercialized applications, the scarcity and high price make them unsuitable for large-scale application [5]. In view of this, great efforts have been devoted to developing cost-effective and highly stable non-/low-noble metal bifunctional electrocatalysts for both ORR and OER in the commercialization of energy devices.

Recently, different kinds of transition metal-based electrocatalysts, such as transition-metal oxides [6], sulfides [7], nitrides [8], *etc.*, have been explored as potential alternative electrocatalysts to Pt in energy conversion and storage applications. Among these advanced materials, bimetallic-based materials, including CoFe [2], NiCo [9], and FeNi [10] catalysts have gained particular attention as they are comparatively cheaper and more abundant. Specially, carbon nanotubes (CNTs) based hybrid materials with outstanding electron transfer kinetics and excellent anti-poisoning performance are among some of the most promising electrocatalysts [11]. In addition, heteroatom co-doping of CNTs (*e.g.*, B–N [12], N–S [13], and N–P [14]) can induce favourable electronic and structural modulations, resulting in further enhanced electrocatalytic activities. Yu et al., developed a novel synthesis of Co nanoislands rooted on Co–N–C nanosheets supported by carbon felts (Co/Co–N–C) catalyst that show a synergistic effect of metal Co islands with OER activity and Co–N–C nanosheets with superior ORR performance. As a result, the ZAB fabricated using optimized catalyst resulted a small charge–discharge voltage gap (0.82 V@10 mA cm^{-2}) and high power density of 132 mW cm^{-2} over performing Pt/C [3]. However, to the best of our knowledge, there is no report on bimetallic Zn–Co decorating N–S-doped tubular structural carbon catalyst for both ORR and OER applications. This observation inspired us to investigate this electrocatalyst design concept as a possible route to better electrocatalysis for rechargeable ZAB.

Herein, we report a template-free chemical approach for *in-situ* growth of bimetallic Zn–Co co-modified N–S-doped tubular structural carbon by a facile pyrolysis method using metal salts (cobalt nitrate and zinc nitrate) as metal precursors, sulphuric acid as sulfur source, and both guanine and melamine as carbon and nitrogen sources. The resulting catalyst demonstrated efficient ORR performance with onset potential of 0.98 V and half-wave potential of 0.87 V at a rotational speed of 1600 rpm with a scan rate of 5 mV s^{-1}, which is better than that of Pt/C and many other reported catalysts [15,16]. The control experiments performed on single-metal samples indicate that the bimetal-related species play a key role in the enhanced ORR activity. The co-contribution from the Co metal particles, Zn–N/Co–N active sites and N/S co-doped tubular structural carbon are proposed to account for the excellent ORR activity. In addition, the composite catalyst also exhibits excellent OER catalytic performance. Furthermore, a primary rechargeable Zn-air battery was assembled using the Zn–Co decorated N–S co-doped tubular structural carbon as the cathode (or as an anode during charging). The rechargeable battery exhibited a steady open-circuit voltage of around 1.50 V and a better performance as compared to that of Pt/C catalyst in various aspects.

2. Experimental section

2.1. Synthesis of x-Zn-Co-N/S–C composites

All chemicals are of analytical grade and can be used directly. Typically, different mass of zinc nitrate hexahydrate [$Zn(NO_3)_2 \cdot 6H_2O$] and cobalt nitrate hexahydrate [$Co(NO_3)_2 \cdot 6H_2O$] (mass ratio of 1:1) were firstly dissolved in a mixed solution containing 10 mL ethanol and 2 mL 0.5 M H_2SO_4. Then, 1.0 g guanine and 1.0 g melamine were added into the above mixture with stirring for 10 min. The uniformly dispersed mixture was dried at 60 °C in an oven and then grounded by agate mortar to obtain fine powders. After that, the powders were placed into a furnace under N_2 atmosphere. The temperature was increased to 900 °C with a heating rate of 2 °C min^{-1} and dwelled for 3 h. The as-prepared pyrolysis catalysts were designated as *x-Zn-Co-N/S–C* (*x* is the total mass of metal salts). The synthesized sample was directly used as electrocatalyst without any post-treatment. For comparison, the S-free, Zn-free, and Co-free samples were synthesized in a similar way without the addition of H_2SO_4, $Zn(NO_3)_2 \cdot 6H_2O$, or $Co(NO_3)_2 \cdot 6H_2O$, respectively. Moreover, the Zn–Co–N/S–C (T) obtained at different temperatures was also prepared in a similar way. The optimal sample in this work was denoted as 0.3-Zn-Co-N/S–C. The contents of Zn and Co in different samples were determined by ICP-MS (Table S1). Most of the Zn was volatilized at 900 °C, and a small part is present in the form of Zn–N. It is hard to detect the corresponding crystal structure of Zn–N species by XRD. The atomic ratio of Zn/Co of 0.3-Zn-Co-N/S–C at different temperatures has also been calculated as shown in Table S1. The atomic ratio of Zn/Co decreases from 1.65 to 0.68 and 0.11 with increasing temperatures (800 °C, 900 °C, and 1000 °C). The optimal Zn/Co ratio is 0.68 at a pyrolysis temperature of 900 °C in terms of ORR performance.

2.2. Preparation of catalytic electrode

The working electrode was polished with 0.05 μm alumina powder and rinsed with water, 0.5 M H_2SO_4 and ethanol for 3 times, respectively. In a typical procedure, 4 mg of catalysts and 10 μL of Nafion solution (5 wt%, DuPont) were added into 1 mL of isopropanol and deionized water (DIW) solution ($V_{isopropanol}$: V_{DIW} = 1 : 1) and then ultrasonicated for ∼ 0.5 h to prepare a homogeneous slurry. Finally, 19.6 μL of the catalysts was coated onto the RRDE electrode using pipette (catalyst loading: ~0.318 mg cm^{-2}) and dried naturally to form a homogeneous membrane.

The kinetic parameters, kinetic current densities, hydrogen peroxide yields and electron transfer numbers for ORR were calculated and discussed in detail in supporting experimental section.

2.3. Electrochemical measurements

All the electrochemical measurements of ORR performance were performed at ∼25 °C with a Pine Modulated Speed Rotator (Pine Research Instrumentation, Inc.). We selected the rotating ring-disk electrode (RRDE) modified with different catalysts as the working electrode, carbon rod as the auxiliary electrode, and Ag/AgCl saturated with KCl as the reference electrode, respectively. All the reported potentials were calibrated with respect to the reversible hydrogen electrode (RHE) of E(RHE) = E(Ag/AgCl) + 0.96 V (Fig. S1). For the ORR, the cyclic voltammetry (CV) measurements were carried out in O_2/N_2-saturated 0.1 M KOH solution at ∼25 °C with a scan rate of 50 mV s^{-1}. The linear sweep voltammetry (LSV) measurements were performed in O_2-saturated 0.1 M KOH solution at different rotating rate

from 400 to 2025 rpm.

The methanol poisoning measurements were recorded by chronoamperometric response in O_2-saturated KOH solution at a rotation speed of 1600 rpm with adding 3.0 M methanol at 200 s. The stability tests were carried out by chronoamperometric technique at a rotation rate of 1600 rpm in O_2-saturated electrolyte for 35000 s.

The OER measurements were operated in O_2-saturated 1 M KOH (pH = 13.9) electrolyte. The LSV recorded at a scan rate of 5 mV s^{-1} and the long-term stability test was performed through controlled potential chronoamperometry measurement.

2.4. Zn-air battery measurements

For Zn−air batteries measurements, the catalysts slurry was obtained in the same procedure to that of ORR test and the air cathode was obtained by loading catalysts slurry on hydrophobic carbon fiber paper (2.0 mg cm^{-2}). The homemade Zn-air batteries were constructed, in which the 6.0 M KOH and 0.2 M $Zn(OAc)_2$ solution acted as electrolyte with polished Zn foil as anode.

3. Results and discussion

3.1. Synthesis strategy and microstructure analysis

The formation of Zn–Co–N/S–C is proposed in Fig. 1a. The sample was synthesized through a facile annealing of a mixture containing H_2SO_4, Zn^{2+}, Co^{2+}, melamine, and guanine at 900 °C under inert atmosphere. The biomass-derived layered molecules, guanine and melamine, were catalyzed by Zn–Co dual sites to transform from layered structure into N-doped tubular structural carbon, while S from sulfur acid was also doped into the carbon at the same time. These tubular structures grew further with the Zn–Co dual sites embedded inside the tubular carbon.

Morphologies of 0.3-Zn-Co-N/S–C were obtained from scanning electron microscopy (SEM) and transmission electron microscopy (TEM). As shown in Fig. 1b, the 0.3-Zn-Co-N/S–C material is composed of a large density of tubular carbon architectures of average diameter ~200 nm. The TEM image in Fig. 1c further confirms the presence of tubular structural carbon architectures. The high-resolution TEM image (inset Fig. 1c) reveals the obvious lattice fringe of 0.20 nm, indexing to

the (220) lattice plane of Co. The Co nanoparticle was wrapped by the outside carbon layer, which exhibited a lattice fringe of 0.32 nm, corresponding to the (002) lattice plane of graphitic carbon. The Co nanoparticles encapsulated by graphite layer could effectively avoid agglomeration and improve the catalytic stability [17]. The high-angle annular dark field scanning transmission electron microscopy (HADDF-STEM) image and the corresponding elemental mappings in Fig. S2 further confirm the composition and elemental distribution of the catalysts. The C, N, and Zn elements are uniformly distributed throughout the tubular structure, while the Co and S were concentrated at the end of the carbon nanotube, somewhat similar to the observation of Co capping in carbon nanotubes where the Co mediates the growth of the carbon nanotubes [18]. Furthermore, the SEM (Fig. S3) images of the 0.3-Zn-Co-N/S–C before and after the ORR and OER stability tests show that the morphology of 0.3-Zn-Co-N/S–C still maintains a tubular structure and without apparent destruction after the stability tests. XRD patterns in Fig. 1d and Fig. S4a reveal a typical peak located at about 26.4° for all samples, corresponding to the (002) plane of graphitic carbon (JCPDS: 41-1487) [19]. The 0.3-Zn-Co-N/S–C, 0.3-Zn-Co-N/C, and Co–N/S–C exhibit α-Co phases (JCPDS: 89-4307) with diffraction peaks at 44.2°, 51.5° and 75.9°, respectively [18]. However, the Zn–N/S–C sample only showed a broad peak of graphitic carbon, indicating the evaporation of Zn metal at about 900 °C, which is in consistent with the results of previous reports [20]. The results of Raman spectra are shown in Fig. 1e, Fig. S4b, and Fig. S5. The intensity ratio of the D-band at 1360 cm^{-1} to the G-band at 1580 cm^{-1} (I_D/I_G) is about 0.98 for 0.3-Zn-Co-N/S–C, reflects the relative higher content of defects of 0.3-Zn-Co-N/S–C than the contrast sample Co–N/S–C (I_D/I_G = 0.93) due to the evaporation of Zn metal under high annealing temperature. Moreover, the high content of defects could also arise from specific doping of N atoms along defective edges [21]. The higher content of graphitic-N observed in XPS (discussed below) for this sample probably reflects this since all N-defects contribute to the I_D band. The I_D/I_G of N/S–C and Zn–N/S–C is 1.01 and 1.10, respectively, which showed more defects and relatively low conductivity (Table S2). Again, the impact of Zn evaporation on the defect levels is apparent from a comparison of these samples (see Fig. S3b). The results in Fig. S5 suggest that the graphitization degree is increased with the increasing pyrolysis temperature in accord with a previous report [22] (Note that there may also be more Zn loss at higher temperatures). Moreover, the
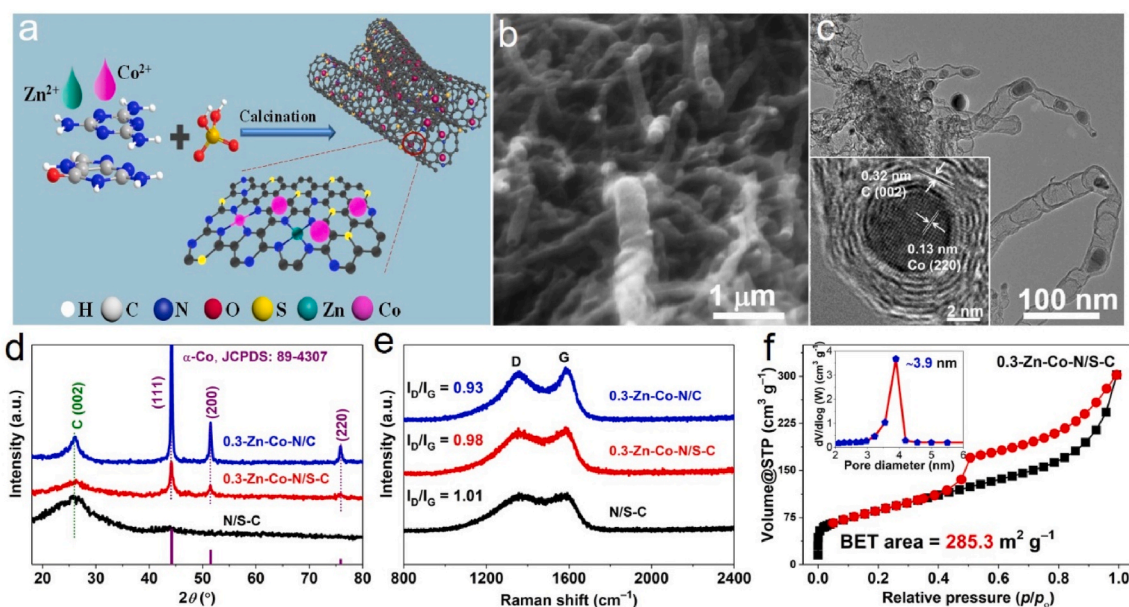
Fig. 1. (a) Synthetic scheme for the preparation of Zn–Co–N/S–C. (b) SEM, (c) TEM (inset: High-resolution TEM), (d) XRD patterns, (e) Raman spectra, and (f) N_2 adsorption-desorption isotherm (inset: pore size distribution curve) of 0.3-Zn-Co-N/S–C.

0.3-Zn-Co-N/S–C shows a large Brunauer-Emmett-Teller (BET) surface area of 285.3 m^2 g^{-1} with average pore diameter of about 3.9 nm (Fig. 1f), suggesting that the 0.3-Zn-Co-N/S–C sample is a mesoporous material [23]. The mesoporous structure helps to expose more active sites and facilitates rapid gas release and electrolyte diffusion [24], thereby significantly enhancing the catalytic activities.

3.2. XPS analysis

The chemical states of the elements in the prepared samples were studied by X-ray photoelectron spectroscopy (XPS). The survey scan (Fig. S6a) of 0.3-Zn-Co-N/S–C confirmed the existence of elemental S, C, N, O, Co and Zn. The high–resolution of C 1s in Fig. S6b can be deconvoluted into four peaks with the binding energy centered at 284.0, 284.6, 286.0 and 288.8 eV, corresponding to C=C, C–C/C–N, C–O/C–S and C=O, respectively [25,26]. Deconvolution of high-resolution S 2p yielded three peaks at 161.1, 162.6, and 167.9 eV are ascribed to the S 2p$_{3/2}$, S 2p$_{1/2}$, and SO$_4^{2-}$, respectively [27] (Fig. S7). The other peaks with the binding energies of 163.6 and 165.1 eV indicate sulfur atoms that replaced the carbon atoms of the pyridine ring, forming the C–S bonds and conjugated C=S bonds [28]. Fig. 2a shows the high-resolution Zn 2p spectrum, with two peaks at 1021.7 eV and 1044.7 eV, attributing to the 2p$_{3/2}$ and 2p$_{1/2}$ electronic states of Zn^{2+}, respectively. The metallic Zn was evaporated. The remaining Zn is in the Zn–N form that is one of the bimetallic sites of the Zn–N/Co–N catalyst [29,30]. To study the effect of Zn^{2+} in 0.3-Zn-Co-N/S–C, the XPS spectra of Co 2p$_{3/2}$ in 0.3-Zn-Co-N/S–C and Co–N/S–C were compared. The Co 2p$_{3/2}$ region of 0.3-Zn-Co-N/S–C is deconvoluted into four peaks at 777.9, 779.6, 781.7 and 784.8 eV corresponding to the metallic Co, Co^{2+}, Co^{3+}, and satellite peaks, respectively [31]. The Co^{2+} peak of 0.3-Zn-Co-N/S–C shifted to lower binding energy compared to that of Co–N/S–C (Fig. 2b), corroborating the higher electronic density of Co active center. It is noteworthy that the metal Co proportion in 0.3-Zn-Co-N/S–C is higher than that in Co–N/S–C, which is beneficial to the faster electronic transmission [23]. Moreover, the peak positions of Co^0, Co^{2+}, Co^{3+} and Zn^{2+} are well maintained without detectable deviation (Fig. S8). Although the overall Co content kept the same before and after ORR and OER tests, the Co chemical state distributions were altered. The higher conductivity of 0.3-Zn-Co-N/S–C from four-point probe meter (RTS-9) further confirms the better charge transfer capability compared to Co–N/S–C and Zn–N/S–C (Table S2), due to the higher Co^0 content in 0.3-Zn-Co-N/S–C. It is generally believed that a portion of the Co^{2+} species coordinates with N to form Co–N active sites in the N-containing composite [32]. The high-resolution N 1s spectra of 0.3-Zn-Co-N/S–C and Co–N/S–C are presented in Fig. 2c, where the N 1s

regions are fitted to the different N moieties. For 0.3-Zn-Co-N/S–C, the fitting yields pyridinic-, pyrrolic-, graphitic-, and oxidized-N at binding energies of 398.1, 399.5, 400.5, and 403.5eV, respectively [20,33]. Pyridinic-, pyrrolic-, and graphitic-N are reported to participate in the hydrogen evolution reaction (HER), ORR, and OER [34,35]. The 0.3-Zn-Co-N/S–C shows higher content of pyridinic-N (49.3%) and graphitic-N (21.7%) than that of Co–N/S–C (48.5% and 15.1%, respectively), likely facilitated by the Zn^{2+} species. As the pyrrolic-N content is almost identical for these samples, it cannot directly explain the differences in catalytic performance discussed below. Furthermore, the pyridinic-N content is also comparable between the samples (0.8% difference); on the other hand, at 6.6%, the difference in graphitic-N content stands out. It is believed that the binding energy of N from the Co–N active sites is very close to the pyridinic-N; therefore, the higher pyridinic-N content often means more Co–N active sites [9].

3.3. Electrochemical analysis

The ORR activities of synthesized catalysts were performed using three-electrode system in 0.1 M KOH solution. Commercial Pt/C was also measured for comparison. The catalysts with the same mass loading of 0.318 mg cm^{-2} were pipetted onto the clean RRDE electrode. Initially, the effects of adding different total mass of Zn(NO$_3$)$_2$·6H$_2$O and Co(NO$_3$)$_2$·6H$_2$O, and different pyrolysis temperatures (800, 900, 1000 °C) were firstly explored. An optimized sample (based on electrochemical performance) was prepared using 0.3 g metal salts (mass ratio of Zn(NO$_3$)$_2$·6H$_2$O and Co(NO$_3$)$_2$·6H$_2$O = 1:1) in the precursor and pyrolysis at 900 °C for 3.0 h. These experimental results of the optimal procedure are presented in Fig. S9 and Fig. S10. One can conclude that the half-wave potential (E$_{1/2}$) increased with the increased dosage of metal salts. However, the E$_{1/2}$ of 0.4-Zn-Co-N/S–C is lower than that of 0.3-Zn-Co-N/S–C, a result of the reduction in the number of active sites due to formation of larger Co nanoparticles. Since the structure of the obtained catalysts is similar, the H$_2$O$_2$ production and electron-transfer number is similar. The effect of pyrolysis temperature on final catalysts shows a similar trend in Fig. S10. For the RRDE results above, control samples were prepared under 900 °C with added metal salt mass of 0.3 g.

Fig. 3a shows the CV profiles of five catalysts in N$_2$- and O$_2$-saturated 0.1 M KOH solutions. In N$_2$-saturated KOH electrolyte, these catalysts showed no cathodic reduction peaks, while distinct oxygen reduction peaks appeared in O$_2$-saturated KOH electrolyte, validating that these catalysts possess intrinsic ORR activities. The oxygen reduction peaks for 0.3-Zn-Co-N/S–C and Co–N/S–C are 0.83 and 0.82 V vs. RHE, respectively, indicating their higher ORR activities than the other
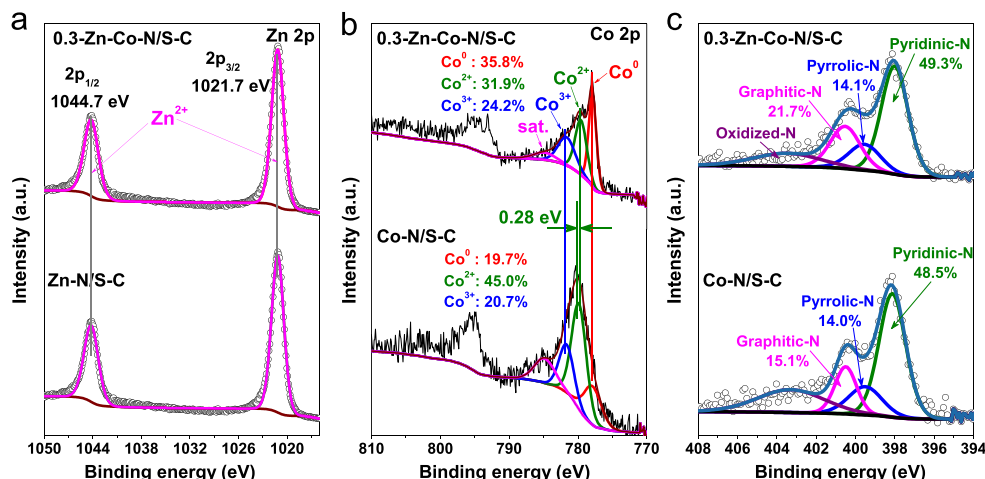
Fig. 2. The corresponding high-resolution Zn 2p (a), Co 2p (b) and N 1s spectra of the samples pyrolyzed at 900 °C.

samples. Fig. 3b displays the RRDE curves for all the samples, including 20 wt% Pt/C, at a rotation speed of 1600 rpm. The half-wave potential ($E_{1/2}$) of 0.3-Zn-Co-N/S–C is 0.87 V, slightly more positive than that of the Pt/C benchmark (0.86 V) as well as those of the comparison samples of this study, indicating its excellent ORR activity. The limiting current density of 0.3-Zn-Co-N/S–C is larger than those of the other samples, perhaps due to the higher content of graphitic N [36]. Moreover, Fig. 3c shows that the Tafel slope of 0.3-Zn-Co-N/S–C is 54.5 mV dec^{-1}, which is substantially lower than that of Pt/C (83.7 mV dec^{-1}) and all comparison samples. Thus, the 0.3-Zn-Co-N/S–C possesses faster ORR kinetics among the synthesized catalysts, related to both its morphology and elemental composition. However, isolating the individual contributions of the different elements is extremely difficult because of the multiple confounding factors between different samples and the well-known synergistic effects within a given sample [37,38]. Accordingly, we only offer a strictly qualitative assessment of the roles of N, S and Co in the ORR performance of 0.3-Zn-Co-N/S–C. The role of Zn has already been inferred above from the XPS results. The evidence for N-defects has already been discussed above, where it was pointed out that graphitic-N ought to play a crucial role in understanding the better ORR performance of 0.3-Zn-Co-N/S–C. With an accurate picture of the relative importance of the different N-defects to ORR activity yet to emerge, the discussion is challenging and can only be tentative. In electrocatalyst design, S is considered an environmental atom, i.e., an atom not directly bonded to the metal center [39]. As already noted, our XPS results show evidence of S replacing C in the pyridine ring to form C–S and C=S bonds, thus altering the charge distribution of the framework. The contribution of S to the ORR activity can be qualitatively inferred from the relative performance between samples 0.3-Zn-Co-N/C and 0.3-Zn-Co-N/S–C. In the absence of S, both the onset potential and limiting current density decrease, while the slope of the Tafel plot increases by 10.5 mV dec^{-1}. These results qualitatively suggest that S has a beneficial impact on the ORR performance of the catalyst consistent with some reports [40,41]. However, the literature indicates that whether the S doping enhances ORR activity depends on a

complex interplay of factors, including doping amount [42], precise site location [43], and the nature of the S functional groups [44]. Note that the vast majority of S doping studies concerned Fe catalyst systems; here we infer a qualitative effectiveness of S doping for a Fe-free dual-metal system.

To explore the role of Co metal in the 0.3-Zn-Co-N/S–C catalyst, the catalyst was treated with nitric acid and hydrochloric acid (volume ratio = 1:3) under 80 °C for 6 h. After centrifugation, washing with abundant deionized water, and drying, we performed the RDE measurement again. As shown in Fig. S11, the $E_{1/2}$ of acid treated sample shows a 40 mV negative shift compared to the initial sample. Moreover, the limiting diffusion current density is smaller than the initial sample. This phenomenon can be ascribed to the partial removal of Co nanoparticles from the catalyst by acid-treatment. This finding qualitatively accords well with the results for N/S–C in Fig. 3(b–d).

The H_2O_2 selectivity and electron transfer-number (n) calculated from RRDE tests demonstrate a nearly four-electron pathway of 0.3-Zn-Co-N/S–C catalyst during the ORR process where the O_2 is transformed directly into OH$^-$, similar to that of 20 wt% Pt/C, over a wide potential range from 0.2 to 0.75 V (Fig. 3d). The RRDE tests at different rotation rates were recorded to further get insight into the ORR mechanism. As shown in Fig. S12a, the current density increases with the increase of rotation speed. It can be seen that the estimated electron transfer number remains at about 3.8 with a H_2O_2 selectivity below 13.0% as the rotation rate increases over a wide potential range (Fig. S12b).

It is reported that larger electrochemical surface area (*ECSA*) catalysts possess abundant active sites [45]. Here, the *ECSA* values of 0.3-Zn-Co-N/S–C, Co–N/S–C, Zn–N/S–C, N/S–C and 0.3-Zn-Co-N/C catalysts are obtained from the calculation of the electrochemical double-layer capacitance (C_{dl}) in 0.1 M KOH solution for the non-Faradaic region [46] (Fig. S13). The largest value of C_{dl} (11.85 mF cm^{-2}) is obtained for 0.3-Zn-Co-N/S–C, suggesting a higher proportion of exposed active sites (Fig. 4a). The surface charge transfer property of these catalysts was further investigated in 0.1 M KCl containing 5 mM $K_3[Fe(CN)_6]$ solution [47]. The CV curves in Fig. S14
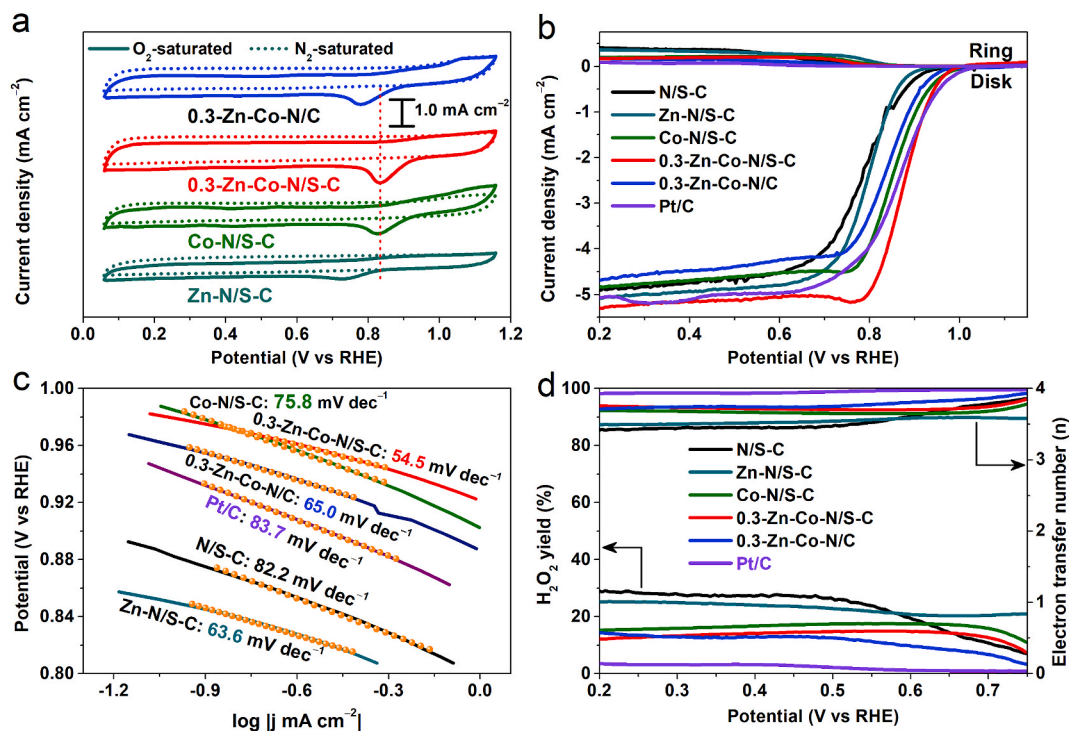
Fig. 3. (a) CV profiles of prepared samples recorded in N$_2$- and O$_2$-saturated KOH solution with scan rate of 50 mV s^{-1}. (b) RRDE voltammograms of different catalysts at a rotation rate of 1600 rpm in an O$_2$-saturated 0.1 M KOH solution at 10 mV s^{-1}. (c) Tafel plots of different catalysts. (d) RRDE tests for H$_2$O$_2$ selectivity and corresponding electron transfer number.

show a pair of redox peaks in which the oxidation peaks are plotted against the square root of the scan rates and is used to evaluate the electron-transfer property by the Randles-Sevcik equation as follows [48]:

$$i_{peak} = \left(2.68 \times 10^5\right) n^{3/2} v^{1/2} A D^{1/2} C_0$$

Where i_{peak} is the peak current, n is the number of electrons involved in the reaction ($n = 1$, Fe^{3+} to Fe^{2+}). v is the scan rate. A is the area (cm^2) of the working electrode. D is the diffusion coefficient of ferricyanide (6.67×10^{-6} cm^2 s^{-1}). C_0 is the concentration of ferricyanide in the bulk solution (mol cm^{-3}).

The electroactive surface area of 0.3-Zn-Co-N/S–C catalyst from this test is *ca.* 0.77 m^2 g^{-1}, which is 2.14- and 1.26-fold higher than those of Zn–N/S–C (0.36 m^2 g^{-1}) and Co–N/S–C (0.61 m^2 g^{-1}) (Fig. 4b), consistent with the C_{dl} results. These results indicate that the process is mainly confined to the surface of electrocatalysts [49]. Hence, the larger C_{dl} value of 0.3-Zn-Co-N/S–C corroborates the observed better ORR performance of this catalyst.

The stability is a vital parameter for evaluating the ORR performance of catalysts. The 0.3-Zn-Co-N/S–C catalyst exhibits excellent long-term stability in 0.1 M KOH solution with only a 3.7% decrease in the current density after 36000 s of reaction, whereas the Pt/C suffers from a greater current decay with only about 66.7% retention over the same period (Fig. 4c). The outstanding durability of 0.3-Zn-Co-N/S–C may be attributed to the formation of N/S doped carbon nanotubes wrapping around Co nanoparticles, protecting the oxidation of Co metal. Another important consideration in the practical application of ORR catalysts is the methanol tolerance. We conducted a methanol tolerance test by injecting 3.0 M methanol to the O_2-saturated 0.1 M KOH solution in the process of chronoamperometric measurements. Fig. 4d demonstrates the excellent methanol tolerance of 0.3-Zn-Co-N/S–C; in contrast, Pt/C shows a sharp drop in performance on adding 3 M CH_3OH. The above results further corroborate the good ORR performance of Zn–Co–N/S–C

and its potential application in fuel cells. However, this catalyst exhibits a weak tolerance to SCN^- poisoning. In the SCN^- poisoning test (Fig. S15), the $E_{1/2}$ of 0.3-Zn-Co-N/S–C is negatively shifted by 5 mV and the gap of current density decreased by 0.97 mA cm^{-2} after adding SCN^-. This notable decline in ORR performance can be ascribed to the SCN^- poisoning of partial Co–N/Zn–N active sites [48,50].

We also studied the electrocatalysts for OER activity. A remarkable OER activity comparable to the RuO_2 benchmark was observed for 0.3-Zn-Co-N/S–C. The LSV curves acquired in 1.0 M KOH (Fig. 5a) highlight the higher OER activity of 0.3-Zn-Co-N/S–C compared to Co–N/S–C, requiring an overpotential of only 440 mV (vs. RHE) to reach the current density of 10 mA cm^{-2}, which is close to that of RuO_2 (290 mV). Meanwhile, a Tafel slope of 89.2 mV dec^{-1} was obtained for 0.3-Zn-Co-N/S–C (Fig. 5b), indicating that the initial electron transfer steps in the sequential $4e^-$ OER reaction are rate-determining [51]. Fig. 5c depicts the gap between the ORR half-wave potential for 0.3-Zn-Co-N/S–C and its OER potential at $j = 10$ mA cm^{-2} to be 0.87 V. It is 80 mV lower than that of Co–N/S–C and 120 mV higher than that of commercial Pt/C‖RuO_2, demonstrating the importance of the porous structure on the improvement OER activity.

3.4. Zinc-air battery analysis

Inspired by the high ORR activity of 0.3-Zn-Co-N/S–C as the air electrode, a primary Zn-air battery was assembled, schematically shown in Fig. 6a. In this electrochemical system, high-purity Zn foil, carbon fiber paper coated with catalysts, and 6.0 M KOH serve as metal-anode, air-cathode, and electrolyte, respectively [52]. In Fig. 6b, the charge and discharge polarization curves show similar charge-discharge voltage gap for the 0.3-Zn-Co-N/S–C and Pt/C + RuO_2, suggesting a great batter recharge ability. As anticipated, the battery exhibits a steady open-circuit voltage of around 1.50 V (Fig. S16), even exceeding that of Pt/C catalyst because of its superior ORR activity. Practical application
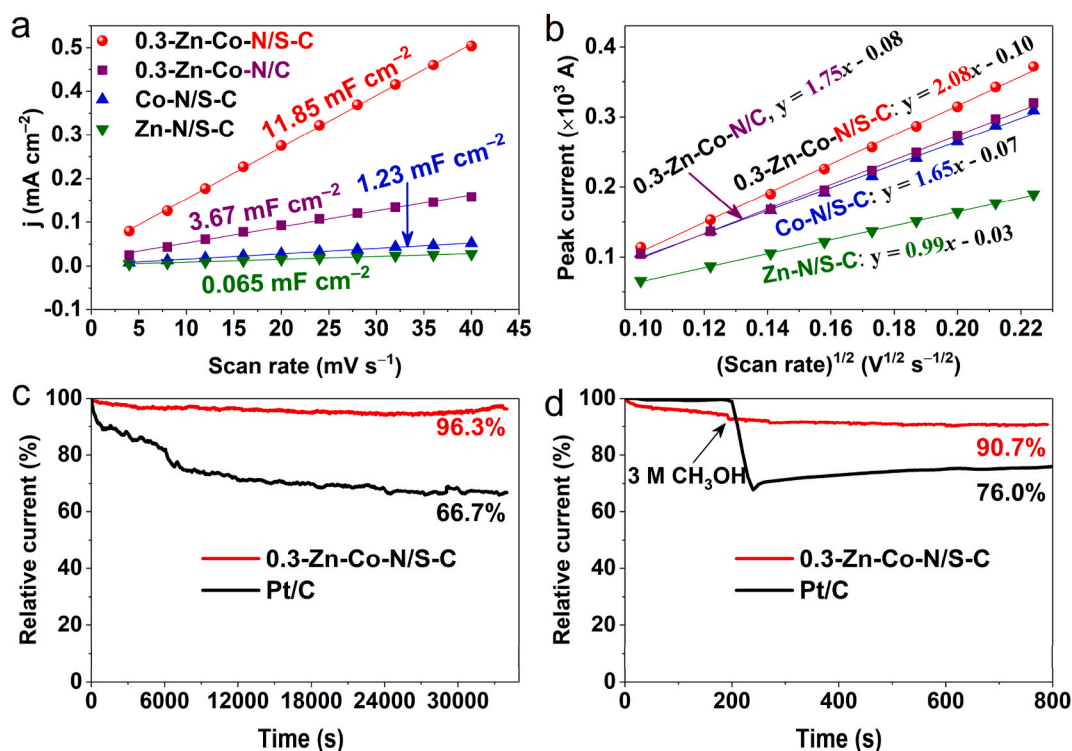
Fig. 4. (a) Plots of current density at 0.25 V (vs. Ag/AgCl). versus scan rates of different catalysts in O_2-saturated 0.1 M KOH. (b) Linear dependence of peak current versus square root of scan rates for different catalysts in 0.1 M KCl containing 5 mM $K_3[Fe(CN)_6]$ solution as a function of scan rate from 10 to 50 mV s^{-1}. (c) Long-term stability test of 0.3-Zn-Co-N/S–C and Pt/C for 34000 s at 0.46 V (vs. RHE) in 0.1 M KOH. (d) Methanol tolerance test of the 0.3-Zn-Co-N/S–C and Pt/C at 0.46 V (vs. RHE) in O_2-saturated KOH (1600 rpm).
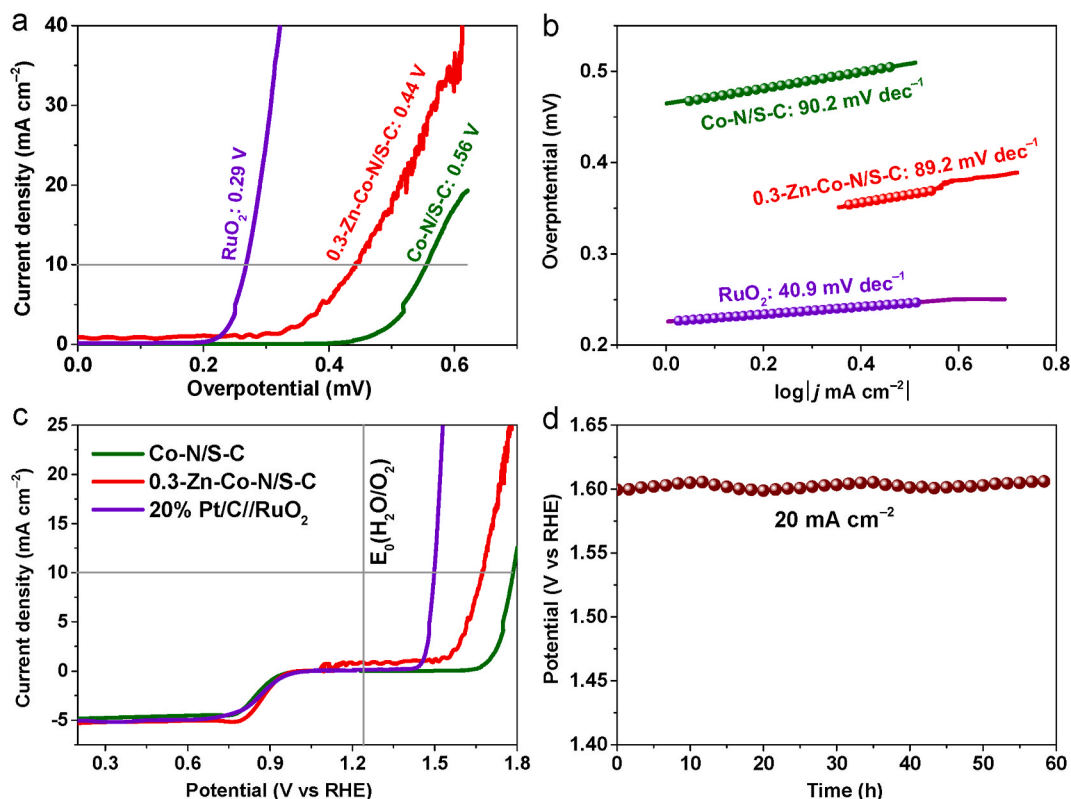
Fig. 5. (a) OER LSV curves of 0.3-Zn-Co-N/S–C and Co–N/S–C in 1.0 M KOH, and (b) the corresponding Tafel plots. (c) LSV curves of different catalysts for both ORR and OER. (d) The stability test for 0.3-Zn-Co-N/S–C at the current density of 20 mA cm^{-2} in 1.0 M KOH.

shows that two self-assembled Zinc-air batteries with 0.3-Zn-Co-N/S–C in series could power the 3.0 V LED lamp (inset: Fig. S16). Moreover, the 0.3-Zn-Co-N/S–C air electrode has a higher working voltage at large current densities (>200 mA cm^{-2}), even surpassing commercial Pt/C + RuO$_2$ cathode. The power density of 0.3-Zn-Co-N/S–C is 129.3 mW cm^{-2}, which is higher than the Pt/C + RuO$_2$ (98.6 mW cm^{-2}) catalyst (Fig. 4c). The result reveals the 0.3-Zn-Co-N/S–C catalyst has a good discharge performance, which is well corresponding to the ORR activity [53]. The Zn-air cells exhibit

stable rate capability without significant decay after discharge at various current densities of 2, 5, 10, 20 mA cm^{-2} (Fig. 6d). It is noted that the discharge platform recovered to 1.31 V when the discharge current density returned to 2.0 mA cm^{-2}. Such a high discharge rate performance emphasizes the excellent reversibility of the Zn-air based on the 0.3-Zn-Co-N/S–C. The 0.3-Zn-Co-N/S–C also endow the Zn–air battery with a higher capacity than Pt/C + RuO$_2$ at 10 mA cm^{-2} based on the consumed Zn weight, *e.g.*, 763 mA h g$_{Zn}^{-1}$ for 0.3-Zn-Co-N/S–C versus 702 mA h g$_{Zn}^{-1}$ for Pt/C + RuO$_2$, as shown in Fig. 6e. The recharge
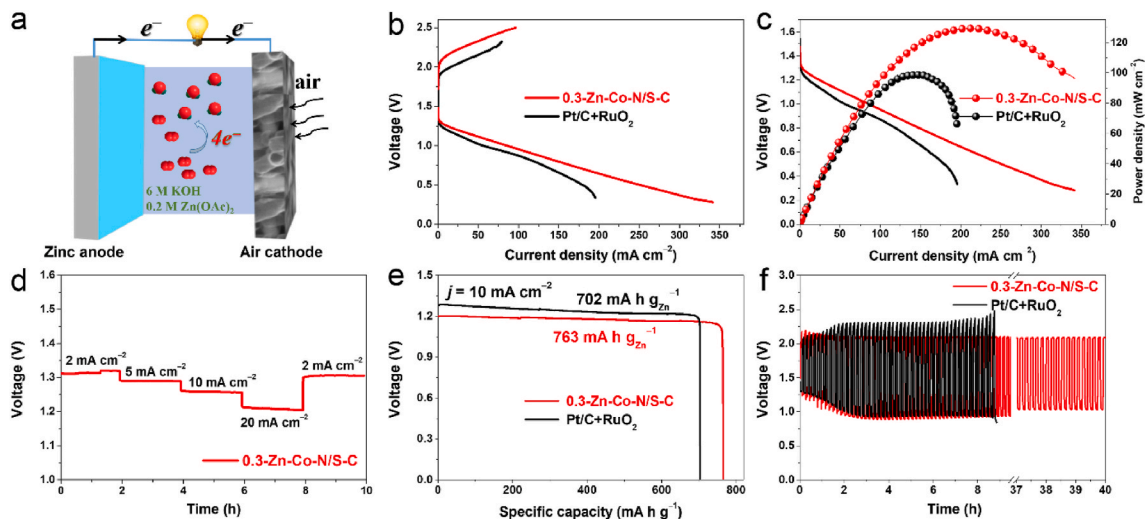
Fig. 6. (a) Schematic configuration of the liquid zinc-air battery. (b) Charge-discharge polarization curves and (c) discharge voltage curves and corresponding power density plot of 0.3-Zn-Co-N/S–C and noble-metal Pt/C + RuO$_2$ tested in the Zn-air batteries. (d) Discharge curves of 0.3-Zn-Co-N/S–C at different current densities. (e) Specific capacity plots at 10 mA cm^{-2}. (f) Galvanostatic discharge and charge voltage profiles of the rechargeable Zn-air batteries at 5 mA cm^{-2} (10 min for each cycle).

ability and cycling stability with 0.3-Zn-Co-N/S–C and Pt/C $+$ RuO$_2$ as air cathode were measured at a current density of 5 mA cm^{-2}. The result in Fig. 6f reveals superb cycle performance of 0.3-Zn-Co-N/S–C without apparent voltage decline after 40 h, suggesting its remarkable cycling stability.

The excellent electrochemical performance of the 0.3-Zn-Co-N/S–C serving as the catalyst of the air-cathode in Zn-air batteries can be attributed to the conductive Co metal nanoparticles and the combination of N/S co-doped carbon nanotubes. First, the incorporation of N/S into the carbon matrix gives rise to apparent changes in the electron distribution on the catalyst, finally reducing the energy barriers of elementary steps during the ORR [54]. Second, the hybrids with the unique carbon nanotube structure can provide efficient electron/ion transportation pathways, shorten the diffusion distance of electrolyte ions, and offer sufficient O$_2$ supply for the active sites [55]. Third, the synergistic effect of the electronic structure and morphology improves the activity of catalysts for the ORR and OER [56]. The above three factors account for the higher electrocatalytic activity and stability of the rechargeable ZAB.

4. Conclusion

In summary, we have constructed a 0.3-Zn-Co-N/S–C self-supported 3D nanostructure through a low-cost and environmentally-friendly method. Our method endows the characteristic of Zn–N/Co–N active sites, highly conductive Co metal nanoparticles, and excellent mass and electron transfer towards rechargeable ZAB. The device exhibits a small charge-discharge voltage gap of 1.1 V at 5 mA cm^{-2}, a higher peak power density, larger discharge capacity at 10 mA cm^{-2} and superior durability up to 40 h without apparent voltage decline. Moreover, it also shows high methanol resistance. XPS and SCN$^-$ results proved that the active sites for ORR have mainly concentrated on Zn and Co species, whereas S–Co–N promotes OER. Overall, the 0.3-Zn-Co-N/S–C self-supported 3D electrocatalyst outperforms the commercial Pt/C catalyst.

CRediT authorship contribution statement

Mancai Qian: Investigation, Methodology. **Meijiao Xu:** Investigation, Data curation. **Man Guo:** Data curation. **Tayirjan Taylor Isimjan:** Writing – review & editing. **Elvis Shoko:** Data curation. **Zhongfeng Shi:** Supervision. **Xiulin Yang:** Supervision, Writing – review & editing.

Declaration of competing interest

The authors declare that they have no known competing financial interests or personal relationships that could have appeared to influence the work reported in this paper.

Acknowledgements

Appendix A. Supplementary data

Supplementary data to this article can be found online at https://doi.org/10.1016/j.jpowsour.2021.230221.

References

[1] D. Yang, L. Zhang, X. Yan, X. Yao, Recent progress in oxygen electrocatalysts for zinc–air batteries, Small Methods 1 (2017) 1700209.

[2] S.L. Zhang, B.Y. Guan, X.W.D. Lou, Co-Fe alloy/N-doped carbon hollow spheres derived from dual metal-organic frameworks for enhanced electrocatalytic oxygen reduction, Small 15 (2019), e1805324.

[3] P. Yu, L. Wang, F. Sun, Y. Xie, X. Liu, J. Ma, X. Wang, C. Tian, J. Li, H. Fu, Co nanoislands rooted on Co–N–C nanosheets as efficient oxygen electrocatalyst for Zn–air batteries, Adv. Mater. 31 (2019) 1901666.

[4] X. Liu, L. Wang, P. Yu, C. Tian, F. Sun, J. Ma, W. Li, H. Fu, A stable bifunctional catalyst for rechargeable zinc-air batteries: iron-cobalt nanoparticles embedded in a nitrogen-doped 3D carbon matrix, Angew. Chem. Int. Ed. 57 (2018) 16166–16170.

[5] Z. Yang, Y. Wang, M. Zhu, Z. Li, W. Chen, W. Wei, T. Yuan, Y. Qu, Q. Xu, C. Zhao, X. Wang, P. Li, Y. Li, Y. Wu, Y. Li, Boosting oxygen reduction catalysis with Fe–N$_4$ sites decorated porous carbons toward fuel cells, ACS Catal. 9 (2019) 2158–2163.

[6] J. Yao, K. Zhang, W. Wang, X. Zuo, Q. Yang, H. Tang, M. Wu, G. Li, Functional integration and self-template synthesis of hollow core-shell carbon mesoporous spheres/Fe$_3$O$_4$/nitrogen-doped graphene to enhance catalytic activity in DSSCs, Nanoscale 10 (2018) 7946–7956.

[7] W. Li, Y. Li, H. Wang, Y. Cao, H. Yu, F. Peng, Co$_9$S$_8$-porous carbon spheres as bifunctional electrocatalysts with high activity and stability for oxygen reduction and evolution reactions, Electrochim. Acta 265 (2018) 32–40.

[8] J. Zhang, J.W. Chen, Y. Luo, Y.H. Chen, X.Y. Wei, G. Wang, R.L. Wang, Sandwich-like electrode with tungsten nitride nanosheets decorated with carbon dots as efficient electrocatalyst for oxygen reduction, Appl. Surf. Sci. 466 (2019) 911–919.

[9] Y. Fu, H.Y. Yu, C. Jiang, T.H. Zhang, R. Zhan, X.W. Li, J.F. Li, J.H. Tian, R.Z. Yang, NiCo alloy nanoparticles decorated on N-doped carbon nanofibers as highly active and durable oxygen electrocatalyst, Adv. Funct. Mater. 28 (2018) 1705094.

[10] P. Song, H. Xu, J. Wang, Y. Zhang, F. Gao, J. Guo, Y. Shiraishi, Y. Du, 1D alloy ultrafine Pt-Fe nanowires as efficient electrocatalysts for alcohol electrooxidation in alkaline media, Nanoscale 10 (2018) 16468–16473.

[11] M. Qiao, S.S. Meysami, G.A. Ferrero, F. Xie, H. Meng, N. Grobert, M.-M. Titirici, Low-cost chitosan-derived N-doped carbons boost electrocatalytic activity of multiwall carbon nanotubes, Adv. Funct. Mater. 28 (2018) 1707284.

[12] J. Yu, C. Wang, W. Yuan, Y. Shen, A. Xie, B, N Co-doped three-dimensional carbon aerogels with excellent electrochemical performance for the oxygen reduction reaction, Chem. Eur J. 25 (2019) 2877–2883.

[13] H. Zeng, W. Wang, J. Li, J. Luo, S. Chen, In situ generated dual-template method for Fe/N/S Co-doped hierarchically porous honeycomb carbon for high-performance oxygen reduction, ACS Appl. Mater. Interfaces 10 (2018) 8721–8729.

[14] D.W. Lee, J.-H. Jang, I. Jang, Y.S. Kang, S. Jang, K.Y. Lee, J.H. Jang, H.-J. Kim, S. J. Yoo, Bio-derived Co$_2$P nanoparticles supported on nitrogen-doped carbon as promising oxygen reduction reaction electrocatalyst for anion exchange membrane fuel cells, Small 15 (2019) 1902090.

[15] J. Wang, X. Zheng, Y. Cao, L. Li, C. Zhong, Y. Deng, X. Han, W. Hu, Developing indium-based ternary spinel selenides for efficient solid flexible Zn-air batteries and water splitting, ACS Appl. Mater. Interfaces 12 (2020) 8115–8123.

[16] S.A. Chala, M.-C. Tsai, W.-N. Su, K.B. Ibrahim, B. Thirumalraj, T.-S. Chan, J.-F. Lee, H. Dai, B.-J. Hwang, Hierarchical 3D architectured Ag nanowires shelled with NiMn-layered double hydroxide as an efficient bifunctional oxygen electrocatalyst, ACS Nano 14 (2020) 1770–1782.

[17] S. Cai, R. Wang, W. Guo, H. Tang, Three-Dimensional macroporous Co-embedded N-doped carbon interweaving with carbon nanotubes as excellent bifunctional catalysts for Zn-air batteries, Langmuir 34 (2018) 1992–1998.

[18] J. Chen, X. Yuan, F. Lyu, Q. Zhong, H. Hu, Q. Pan, Q. Zhang, Integrating MXene nanosheets with cobalt-tipped carbon nanotubes for an efficient oxygen reduction reaction, J. Mater. Chem. A 7 (2019) 1281–1286.

[19] J. Zhang, M. Zhang, L. Qiu, Y. Zeng, J. Chen, C. Zhu, Y. Yu, Z. Zhu, Three-dimensional interconnected core–shell networks with Ni(Fe)OOH and M–N–C active species together as high-efficiency oxygen catalysts for rechargeable Zn–air batteries, J. Mater. Chem. A 7 (2019) 19045–19059.

[20] Z. Meng, S. Cai, R. Wang, H. Tang, S. Song, P. Tsiakaras, Bimetallic−organic framework-derived hierarchically porous Co-Zn-N-C as efficient catalyst for acidic oxygen reduction reaction, Appl. Catal. B Environ. 244 (2019) 120–127.

[21] M. Li, Y. Liu, L. Han, J. Xiao, X. Zeng, C. Zhang, M. Xu, P. Dong, Y. Zhang, A novel strategy for realizing high nitrogen doping in Fe$_3$C-embedded nitrogen and phosphorus-co-doped porous carbon nanowires: efficient oxygen reduction reaction catalysis in acidic electrolytes, J. Mater. Chem. A 7 (2019) 17923–17936.

[22] M. Liu, H. Lin, Z. Mei, J. Yang, J. Lin, Y. Liu, F. Pan, Tuning cobalt and nitrogen Co-doped carbon to maximize catalytic sites on a superabsorbent resin for efficient oxygen reduction, ChemSusChem 11 (2018) 3631–3639.

[23] M. Zhang, C. Wang, X. Yan, K.P. Kwame, S. Chen, C. Xiao, J. Qi, X. Sun, L. Wang, J. Li, Metal organic framework-derived hollow cactus-like carbon sheets for oxygen reduction, J. Mater. Chem. A 7 (2019) 20162–20168.

[24] X.X. Yang, X.L. Hu, X.L. Wang, W. Fu, X.Q. He, T. Asefa, Metal-organic framework-derived Fe$_3$C@NC nanohybrids as highly-efficient oxygen reduction electrocatalysts in both acidic and basic media, J. Electroanal. Chem. 823 (2018) 755–764.

[25] X. Cheng, P. Yan, S. Liu, M. Qian, B. Wang, Z. Wan, J. Tian, X.-C. Shen, T. T. Isimjan, X. Yang, Well-dispersed iron oxide stabilized Fe-N$_4$ active sites in porous N-doped carbon spheres as alternative superior catalyst for oxygen reduction, Int. J. Hydrogen Energy 44 (2019) 12127–12137.

[26] M. Khandelwal, S. Chandrasekaran, S.H. Hur, J.S. Chung, Chemically controlled in-situ growth of cobalt oxide microspheres on N,S-co-doped reduced graphene oxide as an efficient electrocatalyst for oxygen reduction reaction, J. Power Sources 407 (2018) 70–83.

[27] H. Niu, Y. Liu, B. Mao, N. Xin, H. Jia, W. Shi, In-situ embedding MOFs-derived copper sulfide polyhedrons in carbon nanotube networks for hybrid supercapacitor with superior energy density, Electrochim. Acta 329 (2020) 135130.

[28] Y. Zhao, N. Yang, H. Yao, D. Liu, L. Song, J. Zhu, S. Li, L. Gu, K. Lin, D. Wang, Stereodefined codoping of sp-N and S atoms in few-layer graphdiyne for oxygen evolution reaction, J. Am. Chem. Soc. 141 (2019) 7240–7244.

[29] P. Song, M. Luo, X. Liu, W. Xing, W. Xu, Z. Jiang, L. Gu, Zn single atom catalyst for highly efficient oxygen reduction reaction, Adv. Funct. Mater. 27 (2017) 1700802.

[30] F. Li, Y. Bu, G.F. Han, H.J. Noh, S.J. Kim, I. Ahmad, Y. Lu, P. Zhang, H.Y. Jeong, Z. Fu, Q. Zhong, J.B. Baek, Identifying the structure of Zn-N$_2$ active sites and structural activation, Nat. Commun. 10 (2019) 2623.

[31] T. Liu, L. Wang, T. Huang, A. Yu, Well-defined carbon nanoframes containing bimetal-N-C active sites as efficient bi-functional electrocatalysts for Li-O$_2$ batteries, Nano Res 12 (2019) 517–523.

[32] J. Li, S. Lu, H. Huang, D. Liu, Z. Zhuang, C. Zhong, ZIF-67 as continuous self-sacrifice template derived NiCo$_2$O$_4$/Co,N-CNTs nanocages as efficient bifunctional electrocatalysts for rechargeable Zn–air batteries, ACS Sustain. Chem. Eng. 6 (2018) 10021–10029.

[33] J. Li, N. Zhou, J. Song, S. Fu, J. Yan, Y. Tang, H. Wang, Cu–MOF-Derived Cu/Cu$_2$O nanoparticles and CuN$_x$C$_y$ species to boost oxygen reduction activity of Ketjenblack carbon in Al–air battery, ACS Sustain. Chem. Eng. 6 (2017) 413–421.

[34] Z. Guo, Z. Zhang, Z. Li, M. Dou, F. Wang, Well-defined gradient Fe/Zn bimetal organic framework cylinders derived highly efficient iron- and nitrogen- codoped hierarchically porous carbon electrocatalysts towards oxygen reduction, Nano Energy 57 (2019) 108–117.

[35] H. Ning, G. Li, Y. Chen, K. Zhang, Z. Gong, R. Nie, W. Hu, Q. Xia, Porous N-doped carbon-encapsulated CoNi alloy nanoparticles derived from MOFs as efficient bifunctional oxygen electrocatalysts, ACS Appl. Mater. Interfaces 11 (2019) 1957–1968.

[36] J. Zhang, G. Chen, K. Müllen, X. Feng, Carbon-Rich nanomaterials: fascinating hydrogen and oxygen electrocatalysts, Adv. Mater. 30 (2018) 1800528.

[37] Y. Chen, S. Ji, S. Zhao, W. Chen, J. Dong, W.-C. Cheong, R. Shen, X. Wen, L. Zheng, A.I. Rykov, S. Cai, H. Tang, Z. Zhuang, C. Chen, Q. Peng, D. Wang, Y. Li, Enhanced oxygen reduction with single-atomic-site iron catalysts for a zinc-air battery and hydrogen-air fuel cell, Nat. Commun. 9 (2018) 5422.

[38] B.-Q. Li, C.-X. Zhao, J.-N. Liu, Q. Zhang, Electrosynthesis of hydrogen peroxide synergistically catalyzed by atomic Co–n$_x$–C sites and oxygen functional groups in noble-metal-free electrocatalysts, Adv. Mater. 31 (2019) 1904044.

[39] C.-X. Zhao, B.-Q. Li, J.-N. Liu, Q. Zhang, Intrinsic electrocatalytic activity regulation of M–N–C single-atom catalysts for oxygen reduction reaction, Angew. Chem. Int. Ed. 60 (2021) 4448–4463.

[40] Y.-C. Wang, Y.-J. Lai, L. Song, Z.-Y. Zhou, J.-G. Liu, Q. Wang, X.-D. Yang, C. Chen, W. Shi, Y.-P. Zheng, M. Rauf, S.-G. Sun, S-doping of an Fe/N/C ORR catalyst for polymer electrolyte membrane fuel cells with high power density, Angew. Chem. Int. Ed. 54 (2015) 9907–9910.

[41] P. Chen, T. Zhou, L. Xing, K. Xu, Y. Tong, H. Xie, L. Zhang, W. Yan, W. Chu, C. Wu, Y. Xie, Atomically dispersed iron–nitrogen species as electrocatalysts for bifunctional oxygen evolution and reduction reactions, Angew. Chem. Int. Ed. 56 (2017) 610–614.

[42] Q. Li, W. Chen, H. Xiao, Y. Gong, Z. Li, L. Zheng, X. Zheng, W. Yan, W.-C. Cheong, R. Shen, N. Fu, L. Gu, Z. Zhuang, C. Chen, D. Wang, Q. Peng, J. Li, Y. Li, Fe isolated single atoms on S, N codoped carbon by copolymer pyrolysis strategy for highly efficient oxygen reduction reaction, Adv. Mater. 30 (2018) 1800588.

[43] H. Shen, E. Gracia-Espino, J. Ma, K. Zang, J. Luo, L. Wang, S. Gao, X. Mamat, G. Hu, T. Wagberg, S. Guo, Synergistic effects between atomically dispersed Fe−N−C and C−S−C for the oxygen reduction reaction in acidic media, Angew. Chem. Int. Ed. 56 (2017) 13800–13804.

[44] Y. Mun, S. Lee, K. Kim, S. Kim, S. Lee, J.W. Han, J. Lee, Versatile strategy for tuning ORR activity of a single Fe-N$_4$ site by controlling electron-withdrawing/donating properties of a carbon plane, J. Am. Chem. Soc. 141 (2019) 6254–6262.

[45] Z. Zou, T. Wang, X. Zhao, W.-J. Jiang, H. Pan, D. Gao, C. Xu, Expediting in-situ electrochemical activation of two-dimensional metal–organic frameworks for enhanced OER intrinsic activity by iron incorporation, ACS Catal. 9 (2019) 7356–7364.

[46] C. Hegde, X. Sun, H. Ren, A. Huang, D. Liu, B. Li, R. Dangol, C. Liu, S. Li, H. Li, Q. Yan, NiAg$_{0.4}$ 3D porous nanoclusters with epitaxial interfaces exhibiting Pt like activity towards hydrogen evolution in alkaline medium, Nanoscale 12 (2020) 8432–8442.

[47] R. Nandan, S. Nanda, Cyanogenic glycosides: a sustainable carbon and nitrogen source for developing resilient Janus reversible oxygen electrocatalysts for metal-air batteries, Carbon 155 (2019) 155–165.

[48] M. Qian, X. Cheng, T. Sun, J. Tian, T.T. Isimjan, Z. Shi, X. Yang, Synergistic catalytic effect of N-doped carbon embedded with CoFe-rich CoFe$_2$O$_4$ clusters as highly efficient catalyst towards oxygen reduction, J. Alloys Compd. 819 (2020) 153015.

[49] Z. Hamoudi, A. Brahim, M.A. ElKhakani, M. Mohamedi, Electroanalytical study of methanol oxidation and oxygen reduction at carbon nanohorns-Pt nanostructured electrodes, Electroanalysis 25 (2013) 538–545.

[50] M. Qian, M. Xu, S. Zhou, J. Tian, T. Taylor Isimjan, Z. Shi, X. Yang, Template synthesis of two-dimensional ternary nickel-cobalt-nitrogen co-doped porous carbon film: promoting the conductivity and more active sites for oxygen reduction, J. Colloid Interface Sci. 564 (2020) 276–285.

[51] J. Hu, X. Yuan, C. Wang, X. Shao, B. Yang, A. Abdul Razzaq, X. Zhao, Y. Lian, Z. Deng, M. Chen, Y. Peng, Self-phosphorization of MOF-armored microbes for advanced energy storage, Small 16 (2020) 2000755.

[52] D.C. Nguyen, D.T. Tran, T.L.L. Doan, D.H. Kim, N.H. Kim, J.H. Lee, Rational design of Core@shell structured CoS$_x$@Cu$_2$MoS$_4$ hybridized MoS$_2$/N,S-codoped graphene as advanced electrocatalyst for water splitting and Zn-air battery, Adv. Energy Mater. 10 (2020) 1903289.

[53] J.H. Park, C.H. Lee, J.-M. Ju, J.-H. Lee, D. Yim, C. Choi, P.V. Braun, S.U. Lee, J.-H. Kim, Molecular engineering of nanostructures and activities on bifunctional oxygen electrocatalysts for Zinc-air batteries, Appl. Catal. B Environ. 270 (2020) 118869.

[54] H. Jin, H. Zhou, W. Li, Z. Wang, J. Yang, Y. Xiong, D. He, L. Chen, S. Mu, In situ derived Fe/N/S-codoped carbon nanotubes from ZIF-8 crystals as efficient electrocatalysts for the oxygen reduction reaction and zinc–air batteries, J. Mater. Chem. A 6 (2018) 20093–20099.

[55] Y. Wang, L. Wang, M. Tong, X. Zhao, Y. Gao, H. Fu, Co–VN encapsulated in bamboo-like N-doped carbon nanotubes for ultrahigh-stability of oxygen reduction reaction, Nanoscale 10 (2018) 4311–4319.

[56] N. Xu, Q. Nie, L. Luo, C. Yao, Q. Gong, Y. Liu, X.-D. Zhou, J. Qiao, Controllable hortensia-like MnO$_2$ synergized with carbon nanotubes as an efficient electrocatalyst for long-term metal–air batteries, ACS Appl. Mater. Interfaces 11 (2019) 578–587.